

Most of the photons that reionized the Universe came from dwarf galaxies

<https://doi.org/10.1038/s41586-024-07043-6>

Received: 16 August 2023

Accepted: 8 January 2024

Published online: 28 February 2024

 Check for updates

Hakim Atek¹✉, Ivo Labbé², Lukas J. Furtak³, Iryna Chemerynska¹, Seiji Fujimoto⁴, David J. Setton⁵, Tim B. Miller⁶, Pascal Oesch^{7,8}, Rachel Bezanson⁵, Sedona H. Price⁵, Pratika Dayal⁹, Adi Zitrin², Vasily Kokorev⁹, John R. Weaver¹⁰, Gabriel Brammer⁹, Pieter van Dokkum¹¹, Christina C. Williams^{12,13}, Sam E. Cutler¹⁰, Robert Feldmann¹⁴, Yoshinobu Fudamoto^{15,16}, Jenny E. Greene¹⁷, Joel Leja^{18,19,20}, Michael V. Maseda²¹, Adam Muzzin²², Richard Pan²³, Casey Papovich^{24,25}, Erica J. Nelson²⁶, Themiya Nanayakkara², Daniel P. Stark¹³, Mauro Stefanon²⁷, Katherine A. Suess^{28,29}, Bingjie Wang^{18,19,20} & Katherine E. Whitaker^{3,10}

The identification of sources driving cosmic reionization, a major phase transition from neutral hydrogen to ionized plasma around 600–800 Myr after the Big Bang^{1–3}, has been a matter of debate⁴. Some models suggest that high ionizing emissivity and escape fractions (f_{esc}) from quasars support their role in driving cosmic reionization^{5,6}. Others propose that the high f_{esc} values from bright galaxies generate sufficient ionizing radiation to drive this process⁷. Finally, a few studies suggest that the number density of faint galaxies, when combined with a stellar-mass-dependent model of ionizing efficiency and f_{esc} , can effectively dominate cosmic reionization^{8,9}. However, so far, comprehensive spectroscopic studies of low-mass galaxies have not been done because of their extreme faintness. Here we report an analysis of eight ultra-faint galaxies (in a very small field) during the epoch of reionization with absolute magnitudes between $M_{\text{UV}} \approx -17$ mag and -15 mag (down to $0.005L^*$ (refs. 10,11)). We find that faint galaxies during the first thousand million years of the Universe produce ionizing photons with $\log[\xi_{\text{ion}} (\text{Hz erg}^{-1})] = 25.80 \pm 0.14$, a factor of 4 higher than commonly assumed values¹². If this field is representative of the large-scale distribution of faint galaxies, the rate of ionizing photons exceeds that needed for reionization, even for escape fractions of the order of 5%.

We combine ultra-deep James Webb Space Telescope (JWST) imaging data with ancillary Hubble Space Telescope (HST) imaging data of the gravitational lensing cluster Abell 2744 (A2744) to photometrically select extremely faint galaxy candidates in the epoch of reionization. A crucial component of our study is the use of strong gravitational lensing to amplify the intrinsically faint flux of distant sources. An accurate estimate of the magnification factor is required to retrieve the intrinsic luminosity of sources. This step relies on a good knowledge of the total mass distribution in the galaxy cluster. Here we use the most recent lensing model (v.1.1) published for the UNCOVER (Ultradep

NIRSpec and NIRCam Observations before the Epoch of Reionization) survey. The magnification factors for our galaxy sample range from $\mu \approx 2$ to $\mu \approx 27$. The values are reported in Table 1, together with 1σ uncertainties. The second part of the UNCOVER programme consists of ultra-deep follow-up spectroscopy with the NIRSpec instrument. We used the Multi-Shutter Assembly to obtain multi-object spectroscopy in seven pointings, totalling an exposure time ranging from 2.7 h to 17.4 h. Figure 1 shows the position of these sources in the A2744 field with the associated regions of high magnification and the configuration of the NIRSpec slits. Simultaneous spectral fits to the continuum and

¹Institut d’Astrophysique de Paris, CNRS, Sorbonne Université, Paris, France. ²Centre for Astrophysics and Supercomputing, Swinburne University of Technology, Melbourne, Victoria, Australia.

³Physics Department, Ben-Gurion University of the Negev, Be’er Sheva, Israel. ⁴Department of Astronomy, The University of Texas at Austin, Austin, TX, USA. ⁵Department of Physics and Astronomy and PITT PACC, University of Pittsburgh, Pittsburgh, PA, USA. ⁶Center for Interdisciplinary Exploration and Research in Astrophysics (CIERA) and Department of Physics and Astronomy, Northwestern University, Evanston, IL, USA. ⁷Department of Astronomy, University of Geneva, Versoix, Switzerland. ⁸Cosmic Dawn Center (DAWN), Niels Bohr Institute, University of Copenhagen, Copenhagen, Denmark. ⁹Kapteyn Astronomical Institute, University of Groningen, Groningen, The Netherlands. ¹⁰Department of Astronomy, University of Massachusetts, Amherst, MA, USA. ¹¹Department of Astronomy, Yale University, New Haven, CT, USA. ¹²NSF’s National Optical-Infrared Astronomy Research Laboratory, Tucson, AZ, USA. ¹³Steward Observatory, University of Arizona, Tucson, AZ, USA. ¹⁴Institute for Computational Science, University of Zurich, Zurich, Switzerland. ¹⁵Waseda Research Institute for Science and Engineering, Faculty of Science and Engineering, Waseda University, Tokyo, Japan. ¹⁶National Astronomical Observatory of Japan, Tokyo, Japan. ¹⁷Department of Astrophysical Sciences, Princeton University, Princeton, NJ, USA. ¹⁸Department of Astronomy and Astrophysics, The Pennsylvania State University, University Park, PA, USA. ¹⁹Institute for Computational and Data Sciences, The Pennsylvania State University, University Park, PA, USA. ²⁰Institute for Gravitation and the Cosmos, The Pennsylvania State University, University Park, PA, USA. ²¹Department of Astronomy, University of Wisconsin, Madison, WI, USA. ²²Department of Physics and Astronomy, York University, Toronto, Ontario, Canada. ²³Department of Physics and Astronomy, Tufts University, Medford, MA, USA. ²⁴Department of Physics and Astronomy, Texas A&M University, College Station, TX, USA. ²⁵George P. and Cynthia Woods Mitchell Institute for Fundamental Physics and Astronomy, Texas A&M University, College Station, TX, USA. ²⁶Department for Astrophysical and Planetary Science, University of Colorado, Boulder, CO, USA. ²⁷Departament d’Astronomia i Astrofísica, Universitat de València, Valencia, Spain. ²⁸Department of Astronomy and Astrophysics, University of California, Santa Cruz, CA, USA. ²⁹Kavli Institute for Particle Astrophysics and Cosmology and Department of Physics, Stanford University, Stanford, CA, USA. [✉]e-mail: hakim.atek@iap.fr

Table 1 | Summary of the sample properties

Source	RA (J2000)	Dec (J2000)	Exptime (h)	μ	z_{phot}	z_{spec}	$M_{\text{UV}}(\text{AB})$
18924	3.581044	-30.389561	17.4	26.6 ± 7.1	$7.9_{-0.3}^{+0.2}$	7.70	-15.47 ± 0.08
16155	3.582953	-30.395232	17.4	11.1 ± 3.8	$6.7_{-0.1}^{+0.1}$	6.87	-16.29 ± 0.08
23920	3.572830	-30.380026	3.7	3.3 ± 0.1	$6.4_{-0.9}^{+0.4}$	6.00	-16.18 ± 0.10
12899	3.582353	-30.402732	10.2	13.9 ± 0.9	$6.6_{-0.2}^{+0.2}$	6.88	-15.34 ± 0.11
8613	3.600602	-30.410271	2.7	9.3 ± 0.6	$6.5_{-0.1}^{+0.1}$	6.38	-16.97 ± 0.04
23619	3.607272	-30.380578	7.5	1.8 ± 0.2	$6.7_{-0.3}^{+0.2}$	6.72	-16.55 ± 0.16
38335	3.541383	-30.357435	2.7	2.3 ± 0.2	$6.4_{-1.8}^{+2.2}$	6.23	-16.89 ± 0.13
27335	3.625081	-30.375261	7.5	1.4 ± 0.1	$6.9_{-0.1}^{+0.5}$	6.76	-17.17 ± 0.08

The exposure time (Exptime) corresponds to the total of all NIRSpec observations for each source. The magnification factors (μ) are computed at the spectroscopic redshift of the source using the most recent UNCOVER lensing model. We also added systematic uncertainties derived from a comparison with an independent lensing model³⁴. The photometric redshift (z_{phot}) is measured with the Eazy software. The spectroscopic redshift (z_{spec}) is measured from the best msaexp fit. The typical best-fit error is $\sigma_{z_{\text{spec}}} = 0.01$. Absolute magnitude $M_{\text{UV}}(\text{AB})$ is measured in the rest-frame UV using the observed magnitude derived from the UNCOVER photometric catalogue corrected for magnification. RA, right ascension; Dec, declination.

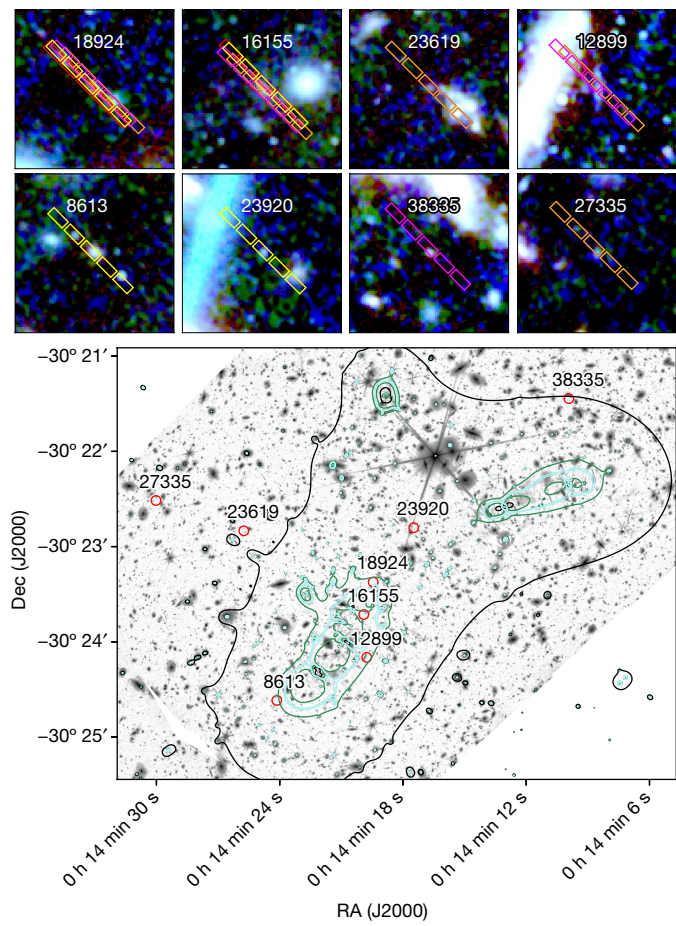
the emission lines provide estimates of the spectroscopic redshifts of these sources, which lie between $z \approx 6$ and $z \approx 7.7$ (Table 1). The spectral extraction and fitting procedure are discussed in the Methods.

Because of the gravitational magnification, we measure extremely faint line fluxes down to $f = 5 \times 10^{-21} \text{ erg s}^{-1} \text{ cm}^{-2}$. We also derive intrinsic absolute magnitudes as faint as $M_{\text{UV}} \lesssim -15.34$ mag, which is nearly two magnitudes fainter than the faintest galaxies discovered in JWST spectroscopic surveys^{13–15} at the epoch of reionization so far (Fig. 2). Assuming a characteristic magnitude of $M_{\text{UV}}^* = -21.15$ mag at $z = 7$, these galaxies are as faint as $0.005L^*$. In light of the steep faint-end slope of the galaxy UV luminosity function at $z > 6$ (refs. 10,16), these galaxies probably provide the bulk of the UV radiation at the epoch of reionization³⁹. To infer the stellar populations of these systems, we perform joint spectrophotometric spectral energy distribution (SED) fits using the Bagpipes (Bayesian Analysis of Galaxies for Physical Inference and Parameter Estimation) software package. Accounting for the magnification, we derive extremely low stellar masses between $\log(M_*/M_{\odot}) = 5.88_{-0.08}^{+0.13}$ and $\log(M_*/M_{\odot}) = 7.12_{-0.08}^{+0.07}$. Our results also show that these galaxies harbour very young stellar populations, with stellar ages mostly around a few million years (Table 2). This picture is also supported by their blue UV continuum slopes, derived from our SED fitting, in the range of $\beta = [-2.07, -2.53]$. These values are generally indicative of a young massive stellar population and low dust attenuation.

The ability of galaxies to reionize the Universe depends on their production of ionizing photon density per unit of time and the fraction of this radiation that escapes to ionize the intergalactic neutral gas. This quantity can be summarized by the following relation: $n_{\text{ion}} = f_{\text{esc}} \xi_{\text{ion}} \rho_{\text{UV}}$, where ρ_{UV} is the non-ionizing UV luminosity density at 1,500 Å, ξ_{ion} is the ionizing photon production efficiency that represents the number of ionizing photons (Lyman continuum photons, LyC) per unit UV luminosity density and f_{esc} is the fraction of this LyC radiation that escapes the galaxy to ionize the intergalactic medium³. It is now well-established that faint galaxies ($M_{\text{UV}} > -18$) are the dominant source of UV radiation during the reionization period^{10,17,18}, although recent JWST observations show several faint active galactic nuclei (AGNs) at $3 < z < 7$ (ref. 19). The ionizing properties of these galaxies, however, are virtually unknown. For example, measurements of their ionizing efficiency ξ_{ion} are challenging even with the deepest JWST spectroscopic surveys, which are limited to galaxies brighter than $M_{\text{UV}} \sim -18$ (ref. 20). We report direct spectroscopic measurements of the ionizing efficiency ξ_{ion} of the faint population of galaxies during the epoch of reionization.

In Fig. 3, we present our ξ_{ion} measurements based on the ratio of the H α recombination line, which is powered by reprocessed ionizing radiation, and the non-ionizing UV luminosity. The most striking

result is the high value of $\log[\xi_{\text{ion}} (\text{Hz erg}^{-1})] = 25.80 \pm 0.14$ observed in faint ($M_{\text{UV}} > -16.5$) galaxies, compared with the canonical value of $\log[\xi_{\text{ion}} (\text{Hz erg}^{-1})] = 25.2$ (ref. 12) commonly assumed in reionization

**Fig. 1 | Layout of the ultra-faint galaxies identified in A2744 cluster field.**

A JWST long-wavelength filters stack (F277W + F356W + F444W) with magnification regions (at $z = 7$) marked with black ($\mu > 2$), green ($\mu > 10$) and cyan ($\mu > 100$) contours, which are derived from the latest lensing model³⁵. The position of each source is marked with a red circle. Two of the sources (12899, 16155) are predicted to be multiply imaged by the lens model, but only the marked image of each system was targeted spectroscopically. On the top of the image, we show an RGB (red, green and blue) image of each source and the positions of each NIRSPEC slitlet on top of the target. RA, right ascension; Dec, declination.

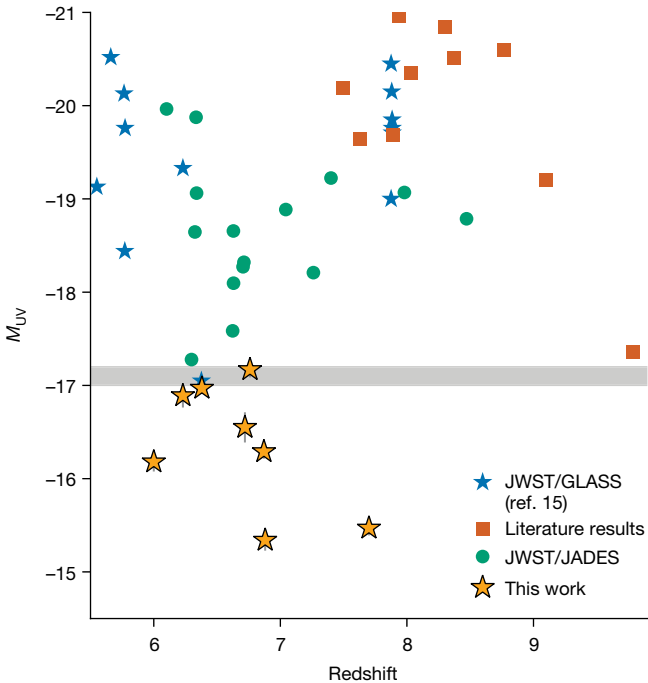


Fig. 2 | Spectroscopic observations of the faintest galaxies during the epoch of reionization. Various literature results from ground-based, HST and JWST observations are shown with orange squares¹⁴. The blue stars represent the spectroscopic sample of the JWST/GLASS (Grism Lens-Amplified Survey from Space) survey presented in ref. 15. The green circles are derived from the latest data release of the deep spectroscopic observations of the JWST/JADES (JWST Advanced Deep Extragalactic Survey) programme¹³. The horizontal grey line denotes the limit of the deepest JWST spectroscopic programmes.

models, or previous studies at this epoch. For example, the measured efficiency in a population of Ly α emitters, which are thought to have larger ionization radiation than the average galaxy population, is around $\log[\xi_{\text{ion}}(\text{Hz erg}^{-1})] = 25.4$ (ref. 21). Our measured value is consistent with the maximum values predicted by the BPASS (Binary Population and Spectral Synthesis)²² stellar population models for a dust-free galaxy with a constant star formation and a stellar age of less than 3 Myr and a $0.1Z_{\odot}$ metallicity. This large ionizing efficiency in faint galaxies implies that modest values of f_{esc} are sufficient for galaxies to reionize the Universe by $z = 6$. Until now, most models of reionization needed to

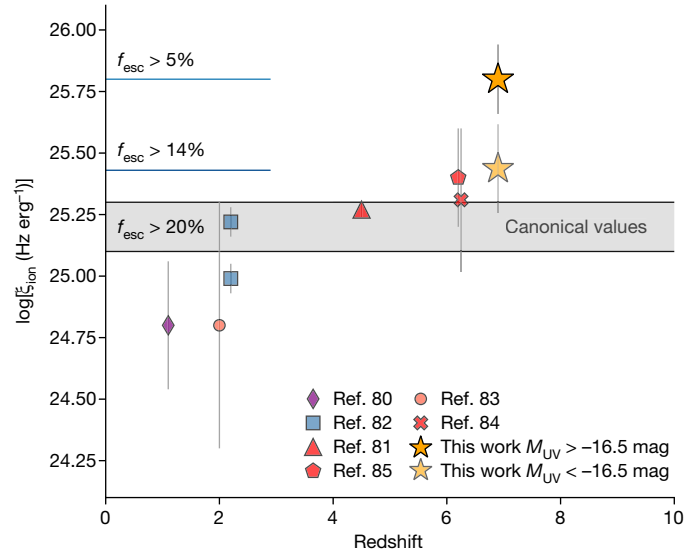


Fig. 3 | The ionizing photon production efficiency of faint galaxies during the epoch of reionization. Our ξ_{ion} measurements are marked with an orange star (light and dark shades for galaxies brighter and fainter than $M_{\text{UV}} = -16.5$, respectively). The grey-shaded horizontal line represents the canonical values assumed when assessing the contribution of galaxies to reionization. Various literature results are also shown and listed in the Methods. Assuming a fiducial UV luminosity density^{10,17}, we plot the minimum f_{esc} required to maintain reionization at each given value of ξ_{ion} (horizontal lines). The error bars represent 1σ uncertainties.

assume large values of f_{esc} , typically around 20%, to accommodate the relatively low ionizing photon emissivity observed in high- z galaxies. Some models required lower f_{esc} values with combinations of specific galaxy properties and a small contribution from AGNs⁸. Direct measurements of f_{esc} $z = 0$ –4 analogues, reported typical or sample-averaged values below 10% (ref. 23), albeit with a large dispersion and higher values have been observed in individual objects. As we can see in Fig. 3, a volume-averaged escape fraction as low as $f_{\text{esc}} = 5\%$ is sufficient for faint galaxies to maintain reionization.

To fully understand cosmic reionization by star-forming galaxies, we compute the spectroscopic UV luminosity function based on the present sample. We put spectroscopic constraints on the prevalence of ultra-faint galaxies. Although with a small sample size, our measurements provide confirmation of the steep faint-end slope of the UV luminosity function at $z \sim 7$, in agreement with the photometric UV luminosity function derived from Hubble Frontier Fields observations²⁴. By integrating this UV luminosity function down to a faint-end limit of $M_{\text{UV}} = -15$ mag, we determine a UV luminosity density of $\log[\rho_{\text{UV}}(\text{erg s}^{-1} \text{Mpc}^{-3})] = 26.22$. Now combining these two quantities, we can obtain the total ionizing emissivity of galaxies for different values of f_{esc} , accounting for the contribution of the ultra-faint population. The result is shown in Fig. 4. Galaxies produce enough ionizing photons to maintain reionization at $z \approx 7$ (ref. 25), assuming on average as little as 5% of this radiation escapes from the galaxies to heat the intergalactic medium. We can go a step further by indirectly estimating f_{esc} using the UV continuum slope we measured for these galaxies. Specifically, we follow an approach pioneered by recent studies of nearby galaxies that calibrated indirect indicators of f_{esc} of LyC emission. In particular, a strong correlation is observed between the observed $\beta_{\text{obs}}^{1.550}$ slope and f_{esc} (ref. 26). Adopting the UV-slope β (Table 2) as a proxy for f_{esc} , we infer escape fractions within $f_{\text{esc}} = [0.045, 0.16]$, well in the range of assumed values in Fig. 4. Another indirect indicator of f_{esc} that has been explored in recent studies is the star-formation surface density Σ_{SFR} (ref. 27). For these compact sources, we measure $\log[\Sigma_{\text{SFR}}/M_{\odot}(\text{yr kpc}^2)] \approx 0.2$ –2. These values are commonly observed in

Table 2 | Summary of the physical properties of the sample derived from SED fitting with Bagpipes

Source	$\log(M_{\star}/M_{\odot})$	$\text{SFR}_{\text{H}\alpha}(M_{\odot} \text{yr})$	$\text{SFR}_{\text{UV}}(M_{\odot} \text{yr})$	β	$t_{50}(\text{Myr})$	$12 + \log(\text{O/H})$
18924	$5.88^{+0.13}_{-0.08}$	0.33 ± 0.02	$0.01^{+0.14}_{-0.07}$	$-2.39^{+0.12}_{-0.10}$	$2.23^{+0.68}_{-0.85}$	6.95 ± 0.15
16155	$6.61^{+0.07}_{-0.06}$	0.92 ± 0.04	$0.04^{+0.08}_{-0.06}$	$-2.09^{+0.07}_{-0.08}$	$3.96^{+0.92}_{-0.66}$	7.01 ± 0.19
23920	$6.30^{+0.03}_{-0.03}$	1.32 ± 0.04	$0.02^{+0.03}_{-0.03}$	$-2.45^{+0.03}_{-0.03}$	$1.12^{+0.32}_{-0.11}$	6.84 ± 0.06
12899	$6.54^{+0.14}_{-0.19}$	0.49 ± 0.02	$0.04^{+0.12}_{-0.15}$	$-2.51^{+0.09}_{-0.07}$	$28.66^{+15.51}_{-11.98}$	6.70 ± 0.15
8613	$7.12^{+0.07}_{-0.08}$	0.78 ± 0.07	$0.16^{+0.08}_{-0.07}$	$-2.53^{+0.04}_{-0.03}$	$25.73^{+6.47}_{-6.33}$	6.97 ± 0.18
23619	$6.57^{+0.10}_{-0.06}$	0.85 ± 0.07	$0.04^{+0.11}_{-0.05}$	$-2.51^{+0.13}_{-0.07}$	$1.08^{+0.22}_{-0.07}$	7.19 ± 0.20
38335	$6.83^{+0.25}_{-0.20}$	1.00 ± 0.16	$0.07^{+0.34}_{-0.15}$	$-2.07^{+0.29}_{-0.24}$	$6.45^{+4.39}_{-2.29}$	7.46 ± 0.32
27335	$6.73^{+0.15}_{-0.08}$	0.73 ± 0.10	$0.05^{+0.17}_{-0.07}$	$-2.35^{+0.22}_{-0.11}$	$1.56^{+1.33}_{-0.52}$	6.99 ± 0.18

For each source, the median posterior and associated uncertainties from the best-fit models are given for the stellar mass ($\log(M_{\star}/M_{\odot})$), the star-formation rate (SFR), the UV continuum slope β and the half-mass age (t_{50}). The oxygen abundance computed from strong optical lines is also reported. The SFR derived from the H α emission is also reported.

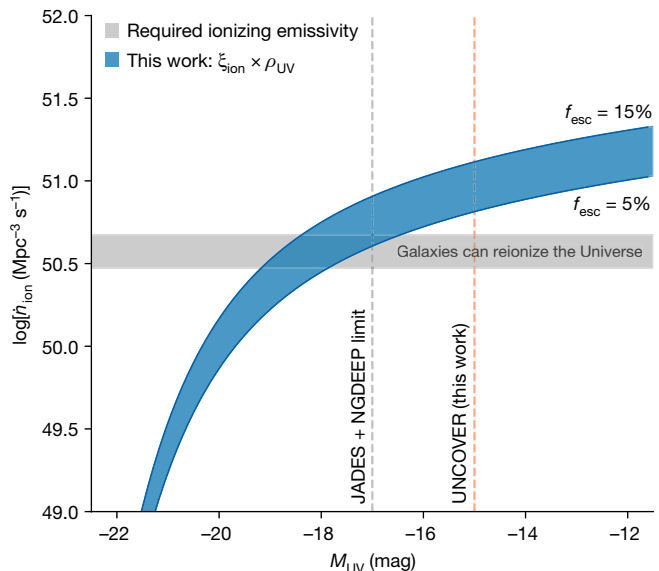


Fig. 4 | The total ionizing emissivity of galaxies at $z = 7$. The total ionizing photon production rate density, derived from the prevalence and the ionizing efficiency of galaxies, as a function of the faint integration limit. The blue region delimits the two cases, in which $f_{\text{esc}} = 5\%$ and $f_{\text{esc}} = 15\%$. The grey-shaded region is the threshold required to maintain the Universe ionized at $z = 7$. The grey vertical line marks the magnitude limit of the deepest JWST spectroscopic surveys to date. The orange vertical line shows the limit probed by this work. At this luminosity, galaxies produce enough radiation to reionize the Universe.

LyC leakers^{28,29} and also predictive of high f_{esc} according to published best-fit relations of $f_{\text{esc}} - \Sigma_{\text{SFR}}$ (ref. 7).

We note that measurements of ξ_{ion} can be markedly affected by dust attenuation. This concern also applies to our estimate of stochastic star formation through the SFR(H α)/SFR(UV) ratio. However, as indicated by the blue UV continuum slopes that we observe, we expect the dust content to be small in these galaxies. This assumption is also supported by the low Balmer decrement H α /H β , for which we measure an average value of 3.3 ± 0.5 . Therefore, dust attenuation should not markedly affect these quantities. We note that we used indirect indicators, which come with a significant scatter, to estimate f_{esc} , because direct measurements of LyC at the epoch of reionization are impossible. The stochastic nature of star formation in these low-mass galaxies also makes the f_{esc} highly variable, because it mainly relies on stellar and supernovae feedback clearing the ISM for LyC escape³⁰. However, on average, hydrodynamical simulations predict higher f_{esc} in lower-mass galaxies^{31,32}. Again, based on the ionizing photon production we estimated, modest values of f_{esc} around 5% are sufficient. We also note that our conclusions are based on observations obtained in one field, and are therefore not immune to field-to-field variations or environmental effects. For instance, the ionizing properties of faint galaxies can be affected differently by reionization radiation if they reside in over-dense regions³³. More observations in an independent field should provide further insights in that regard.

Online content

Any methods, additional references, Nature Portfolio reporting summaries, source data, extended data, supplementary information, acknowledgements, peer review information; details of author contributions and competing interests; and statements of data and code availability are available at <https://doi.org/10.1038/s41586-024-07043-6>.

- Dayal, P. & Ferrara, A. Early galaxy formation and its large-scale effects. *Phys. Rep.* **780–782**, 1–64 (2018).
- Mason, C. A., Naidu, R. P., Tacchella, S. & Leja, J. Model-independent constraints on the hydrogen-ionizing emissivity at $z > 6$. *Mon. Not. R. Astron. Soc.* **489**, 2669–2676 (2019).

- Robertson, B. E. et al. Identification and properties of intense star-forming galaxies at redshifts $z > 10$. *Nat. Astron.* **7**, 611–621 (2023).
- Robertson, B. E. Galaxy formation and reionization: key unknowns and expected breakthroughs by the James Webb Space Telescope. *Annu. Rev. Astron. Astrophys.* **60**, 121–158 (2022).
- Madau, P. & Haardt, F. Cosmic reionization after Planck: could quasars do it all? *Astrophys. J. Lett.* **813**, L8 (2015).
- Mitra, S., Choudhury, T. R. & Ferrara, A. Cosmic reionization after Planck II: contribution from quasars. *Mon. Not. R. Astron. Soc.* **473**, 1416–1425 (2018).
- Naidu, R. P. et al. Rapid reionization by the oligarchs: the case for massive, UV-bright, star-forming galaxies with high escape fractions. *Astrophys. J.* **892**, 109 (2020).
- Finkelstein, S. L. et al. Conditions for reionizing the Universe with a low galaxy ionizing photon escape fraction. *Astrophys. J.* **879**, 36 (2019).
- Dayal, P. et al. Reionization with galaxies and active galactic nuclei. *Mon. Not. R. Astron. Soc.* **495**, 3065–3078 (2020).
- Finkelstein, S. L. et al. The evolution of the galaxy rest-frame ultraviolet luminosity function over the first two billion years. *Astrophys. J.* **810**, 71 (2015).
- Bouwens, R. J. et al. UV luminosity functions at redshifts $z \sim 4$ to $z \sim 10$: 10,000 galaxies from HST legacy fields. *Astrophys. J.* **803**, 34 (2015).
- Robertson, B. E., Ellis, R. S., Furlanetto, S. R. & Dunlop, J. S. Cosmic reionization and early star-forming galaxies: a joint analysis of new constraints from Planck and the *Hubble* Space Telescope. *Astrophys. J. Lett.* **802**, L19 (2015).
- Bunker, A. J. et al. JADES NIRSpec initial data release for the Hubble Ultra Deep Field: redshifts and line fluxes of distant galaxies from the deepest JWST Cycle 1 NIRSpec Multi-Object spectroscopy. Preprint at <https://doi.org/10.48550/arXiv.2306.02467> (2023).
- Roberts-Borsani, G. et al. The nature of an ultra-faint galaxy in the cosmic dark ages seen with JWST. *Nature* **618**, 480–483 (2023).
- Mascia, S. et al. Closing in on the sources of cosmic reionization: first results from the GLASS-JWST program. *Astron. Astrophys.* **672**, A155 (2023).
- Ishigaki, M. et al. Full-data results of *Hubble* Frontier Fields: UV luminosity functions at $z \sim 6$ –10 and a consistent picture of cosmic reionization. *Astrophys. J.* **854**, 73 (2018).
- Atek, H. et al. Are ultra-faint galaxies at $z = 6$ –8 responsible for cosmic reionization? Combined constraints from the *Hubble* Frontier Fields clusters and parallels. *Astrophys. J.* **814**, 69 (2015).
- Bouwens, R. J., Oesch, P. A., Illingworth, G. D., Ellis, R. S. & Stefanon, M. The $z \sim 6$ luminosity function fainter than ~ 15 mag from the *Hubble* Frontier Fields: the impact of magnification uncertainties. *Astrophys. J.* **843**, 129 (2017).
- Matthee, J. et al. Little Red Dots: an abundant population of faint AGN at $z < 5$ revealed by the EIGER and FRESCO JWST surveys. Preprint at <https://doi.org/10.48550/arXiv.2306.05448> (2023).
- Fujimoto, S. et al. CEERS spectroscopic confirmation of NIRCam-selected $z \geq 8$ galaxy candidates with JWST/NIRSpec: initial characterization of their properties. *Astrophys. J. Lett.* **949**, L25 (2023).
- Simmonds, C. et al. The ionizing photon production efficiency at $z \sim 6$ for Lyman-alpha emitters using JEMS and MUSE. *Mon. Not. R. Astron. Soc.* **523**, 5468–5486 (2023).
- Stanway, E. R. & Eldridge, J. J. Re-evaluating old stellar populations. *Mon. Not. R. Astron. Soc.* **479**, 75–93 (2018).
- Pahl, A. J., Shapley, A., Steidel, C. C., Chen, Y. & Reddy, N. A. An uncontaminated measurement of the escaping Lyman continuum at $z \sim 3$. *Mon. Not. R. Astron. Soc.* **505**, 2447–2467 (2021).
- Atek, H., Richard, J., Kneib, J.-P. & Schaerer, D. The extreme faint end of the UV luminosity function at $z \sim 6$ through gravitational telescopes: a comprehensive assessment of strong lensing uncertainties. *Mon. Not. R. Astron. Soc.* **479**, 5184–5195 (2018).
- Gnedin, N. Y. & Madau, P. Modeling cosmic reionization. *Living Rev. Comput. Astrophys.* **8**, 3 (2022).
- Chisholm, J. et al. The far-ultraviolet continuum slope as a Lyman Continuum escape estimator at high redshift. *Mon. Not. R. Astron. Soc.* **517**, 5104–5120 (2022).
- Naidu, R. P. et al. Two remarkably luminous galaxy candidates at $z = 10$ –12 revealed by JWST. *Astrophys. J. Lett.* **940**, L14 (2022).
- Naidu, R. P. et al. The HDUV Survey: six Lyman continuum emitter candidates at $z \sim 2$ revealed by HST UV Imaging. *Astrophys. J.* **847**, 12 (2017).
- Vanzella, E. et al. Direct Lyman continuum and Ly α escape observed at redshift 4. *Mon. Not. R. Astron. Soc.* **476**, L15–L19 (2018).
- Treibtsch, M., Blaizot, J., Rosdahl, J., Devriendt, J. & Slyz, A. Fluctuating feedback-regulated escape fraction of ionizing radiation in low-mass, high-redshift galaxies. *Mon. Not. R. Astron. Soc.* **470**, 224–239 (2017).
- Ma, X. et al. No missing photons for reionization: moderate ionizing photon escape fractions from the FIRE-2 simulations. *Mon. Not. R. Astron. Soc.* **498**, 2001–2017 (2020).
- Yeh, J. Y.-C. et al. The THESAN project: ionizing escape fractions of reionization-era galaxies. *Mon. Not. R. Astron. Soc.* **520**, 2757–2780 (2023).
- Hutter, A., Dayal, P., Legrand, L., Gottlöber, S. & Yepes, G. Astraeus – III. The environment and physical properties of reionization sources. *Mon. Not. R. Astron. Soc.* **506**, 215–228 (2021).
- Bergamini, P. et al. New high-precision strong lensing modeling of Abell 2744. Preparing for JWST observations. *Astron. Astrophys.* **670**, A60 (2023).
- Furtak, L. J. et al. UNCOVERing the extended strong lensing structures of Abell 2744 with the deepest JWST imaging. *Mon. Not. R. Astron. Soc.* **523**, 4568–4582 (2023).

Publisher's note Springer Nature remains neutral with regard to jurisdictional claims in published maps and institutional affiliations.

Springer Nature or its licensor (e.g. a society or other partner) holds exclusive rights to this article under a publishing agreement with the author(s) or other rightsholder(s); author self-archiving of the accepted manuscript version of this article is solely governed by the terms of such publishing agreement and applicable law.

© The Author(s), under exclusive licence to Springer Nature Limited 2024

Methods

Throughout the paper, we use absolute magnitudes³⁶ and a standard cosmology with $H_0 = 70 \text{ km s}^{-1} \text{Mpc}^{-1}$, $\Omega_A = 0.7$ and $\Omega_m = 0.3$.

Observations and sample selection

The UNCOVER dataset consists of both imaging and spectroscopic observations of the lensing cluster A2744. The imaging observations and data reduction are described in detail in the survey and catalogue papers^{37,38}. Here we briefly summarize the imaging and photometric products used in the present paper. HST imaging consists of seven broadband filters (F435W, F606W, F814W, F105W, F125W, F140W and F160W). The NIRCam³⁹ images include short-wavelength broadband filters (F115W, F150W and F200W), long-wavelength broadbands (F277W, F356W and F444W) and one medium-band filter (F410M). Data were processed and drizzled into 0.04 arcsec pixel⁻¹ mosaics using the Grism redshift and line analysis software for space-based spectroscopy⁴⁰ (Grizli; v.1.6.0.dev99). In terms of ancillary data, the Hubble Frontier Fields (HFF) programme⁴¹ has obtained deep optical and NIR observations of the core area of A2744 with the Advanced Camera for Surveys (435W, F606W and F814W), and Wide-Field Camera Three (F105W, F125W, F140W and F160W). A wider area around the cluster has also been covered by the BUFFALO (Beyond Ultra-deep Frontier Fields and Legacy Observations) programme⁴² in almost identical broadband filters (without F435W and F140W). All HST observations were drizzled to the same pixel scale and the same orientation as the NIRCam mosaics.

The second part of the UNCOVER programme consists of ultra-deep follow-up spectroscopy with the NIRSpec instrument⁴³. Data were obtained between 31 July 2023 and 2 August 2023. Observations use the Prism mode and the Multi-Shutter Assembly⁴⁴ of NIRSpec to observe more than 650 targets. To optimize background subtraction, each target was observed with a three-slit nodding strategy. Observations were split into seven pointings, with important overlap at the centre, providing total on-target exposure times ranging from about 2.7–17.4 h. The spectral resolution is wavelength dependent and varies between $R \sim 30$ –300 over the full wavelength range $\lambda \sim 0.6$ –5.3 μm . Data were reduced using the JWST/NIRSpec analysis software msaexp v.0.6.10. The processing is based on level 2 MAST products, using the CRDS context file jwst_1100.pmap. The software performs basic reduction steps, including flat-field, bias, 1/f noise and snowball correction, wavelength and photometric calibrations of individual exposure frames⁴⁵. The extraction of one-dimensional (1D) spectra from individual exposures is operated on an inverse-weighted stack of two-dimensional spectrum in the dispersion direction, following an optimal extraction procedure⁴⁶. Then the software fits a Gaussian profile along the cross-dispersion direction to define the 1D extraction aperture. Finally, we compute the final deep 1D spectrum by performing inverse-variance stacking of the individual spectra. To account for slit loss effects, we apply a wavelength-(broadband-)dependent correction factor to re-scale the 1D spectrum to the observed NIRCam aperture photometry. We show an example of the imaging and spectroscopic data in Extended Data Fig. 1. A clear Lyman break at rest-frame wavelength $\lambda_{\text{rest}} = 1,216 \text{ \AA}$ is observed, together with multiple strong emission lines, including H α + [NII], [OIII] $\lambda\lambda$ 4960, 5008, H β , H γ and [OII] λ 3727.

The selection of our sample combines several criteria to constrain the photometric redshifts of the sources. First, we applied a colour–colour selection, based on a flux dropout in the HST optical filters caused by rest-frame Lyman- α absorption by residual intergalactic hydrogen gas. This selection consolidates most of the sources identified in the HFF data^{24,47} at $6 < z < 9$. Second, we performed an SED fitting with the Eazy⁴⁸ software to estimate photometric redshifts, assuming a flat luminosity prior and the corr_sfzhz library of stellar population templates. The allowed redshift range was set to $0.01 < z < 20$. The sources have been selected to have best-fit photometric solutions lying $6 < z < 9$ at the heart of the epoch of reionization. The final selection was then

performed according to the intrinsic luminosity, combining high magnifications ($\mu \gtrsim 2$) and faint observed luminosities in F150W, resulting in intrinsic absolute UV magnitudes of order $M_{\text{UV}} \gtrsim -17$.

Spectral fitting

To determine the spectroscopic redshift of the sources, we fit spectral templates using msaexp, which is based on the SED fitting software Eazy⁴⁹. The code combines a set of templates to fit simultaneously the continuum, including the Lyman break caused by the intergalactic medium (IGM) absorption and the emission lines. For our analysis, we adopt the corr_sfzhz_13 template library that includes redshift-dependent star-formation histories, which are known to perform better than the default fspz_full library in recovering the true redshift³⁸. We search for the best-fit solution over the redshift interval $0 < z < 15$. The spectroscopic redshifts are reported in Table 2. Once the best-fit redshift is found, we refit the spectra, fixing the redshift to z_{spec} , with a set of spline functions to measure the continuum and Gaussians to measure the emission line fluxes. Examples of the best-fit model plotted over the observed spectrum are presented in Fig. 1.

Strong lensing

We use v.1.1 of the UNCOVER lensing model³⁵, which is publicly available in the latest UNCOVER data release DR-1. The model is based on the parametric approach in a previous study⁵⁰, which has been rewritten to be fully analytic—that is, not limited by a grid-resolution^{35,51}. The UNCOVER lens model of A2744 was constructed on a wealth of ground- and space-based data, including deep HST and JWST imaging, and Multi-unit Spectroscopic Explorer⁵² (MUSE) spectroscopic redshifts of both cluster members and multiple images^{34,53–55}. It comprises 421 cluster member galaxies identified in the approximately 45 arcmin² UNCOVER field-of-view and five smooth cluster-scale dark matter halos. The model is constrained with 141 multiple images belonging to 48 sources and achieves an image reproduction RMS of $\Delta_{\text{RMS}} = 0.51''$ in the lens plane. Owing to the massive cluster substructures identified with UNCOVER³⁵, the critical area of the cluster is 1.5 times larger than that inferred from HFF data and the total source plane area with $\mu > 4$ of about 4 arcmin² for a source at redshift $z_s = 6$. The model uncertainties on the amplification values are derived from a Markov Chain Monte Carlo (MCMC) procedure within the modelling code Zitrin-analytic^{56,57}. The temperatures of the MCMC are chosen to reflect typical systematics inherent to parametric lens modelling techniques⁵⁷. To better estimate systematics uncertainties inherent to models, we used an independent mass model for A2744 (ref. 34) for comparison. The magnification factors are in good agreement within 1σ uncertainties, except for two objects that have a difference at the level of 1.5σ and 2σ . Moreover, the statistical uncertainties derived from each model are of the same order. We have incorporated these systematic uncertainties in the quoted errors on the amplification factors.

Physical properties

Bagpipes. We infer global physical properties from SED fitting using the Bagpipes software package^{58,59}. Before fitting, all models are convolved with the NIRSpec/Prism instrumental resolution curve provided by the Space Telescope Science Institute (jwst_nirspec_Prism_disp.fits), assuming that the flight performance is 1.3 times better than stated and is consistent with an earlier work in which a factor 1/0.7 is introduced for modelling $z > 10$ galaxies⁶⁰. Moreover, we fit with a wavelength-independent velocity smoothing ($0 < \log(v_{\text{smooth}}) < 3.3$) as a nuisance parameter. We adapt the following model grid⁶¹: stellar population models, the MILES spectral library^{62,63}, CLOUDY nebular emission models^{64,65} and dust model (with a V-band attenuation in the range $0 < A_v < 5$ and $0.3 < n < 2.5$ as free parameters). The stellar- and gas-phase metallicity are tied to the same value and also included as a free parameter in the range $-2 < \log(Z/Z_\odot) < 0.3$. The ionization parameter is also left free in the range $-3.5 < \log(U) < -1.0$. We parameterize

Article

the star-formation history as a delayed- τ model ($SFR \propto -t/\tau$, which can flexibly produce rising or falling star-formation histories for this range of τ at the redshift of the sample), with the age ($-3 < \log(\text{age}) < 0.48$) and τ ($0.01 < \tau < 5$) as free parameters. This parameterization has been shown to reliably recover star-formation rates and the mass formed in recent star formation, but it is potentially susceptible to underestimating stellar masses because of outshining by the youngest stellar population⁶⁶. Redshift is restricted to vary in a narrow range around the best-fitting spectroscopic redshifts (± 0.1). We fit for a polynomial calibration vector of order 2 after applying a wavelength-independent calibration to scale the normalization of the spectrum to the photometry. The Bagpipes white noise model is used to allow for underestimated errors up to a factor of 10. A signal-to-noise ceiling of 20 is imposed on both our photometry and spectroscopy to account for systematic issues with flux calibration. Sampling is performed by PyMultinest^{67,68}, with the default Bagpipes convergence criteria. The most important physical properties derived from this procedure are presented in Table 2, and example fits and posteriors are presented in Extended Data Fig. 2.

Apart from the SFR derived from SED fitting, we also compute the SFR based on the H α or H β recombination line. The H α indicator traces massive short-lived stars on a timescale of a few Myr, whereas the UV emission indicates an SFR averaged on a longer timescale up to a few 100 Myr. We report high values for the SFR(H α)/SFR(UV) ratio in the range [5–60], indicating recent bursts of star formation in these young systems. This is in line with their specific star-formation rates (SSFR). Given their low stellar masses, these sources have $\log[\text{SSFR}(\text{H}\alpha) (\text{yr}^{-1})] = [-7.4, -6.2]$, which means that they can double their stellar mass in 2–20 Myr.

BEAGLE. We run an additional spectral fit with the Bayesian Analysis of Galaxy SEDs (BEAGLE) tool⁶⁹ on the magnification-corrected spectra. BEAGLE uses the latest version of the Bruzual and Charlot stellar population synthesis models⁶¹ and nebular emission templates computed with Cloudy^{70,71}. We then assume a Chabrier⁷² initial stellar mass function (IMF), a Small Magellanic Cloud dust attenuation law⁷³, the latest analytic IGM attenuation models⁷⁴ and a delayed exponential star-formation history as for our Bagpipes fit. All other parameters are left free to vary with uniform or log-uniform priors: stellar mass $\log(M/M_\odot) \in [4, 10]$, current (10 Myr) SFR $\log[\psi/M_\odot (\text{yr}^{-1})] \in [-2, 4]$, maximum stellar age $\log[t_{\text{age}} (\text{yr})] \in [6, t_{\text{universe}}]$, star-formation e-folding time $\log[\tau (\text{yr})] \in [5.5, 9.5]$, stellar metallicity $\log(Z/Z_\odot) \in [-2.2, -0.3]$, effective V-band dust attenuation optical depth $\hat{\tau}_V \in [0, 3]$, effective galaxy-wide ionization parameter $\log(U) \in [-4, -1]$, gas-phase metallicity $\log(Z_{\text{gas}}/Z_\odot) \in [-2.2, -0.3]$ and dust-to-metal mass ratio $\xi_d \in [0.1, 0.5]$. The posterior distribution of the physical properties that we derive with BEAGLE agrees well with the Bagpipes results presented in Table 2.

Contribution of galaxies to reionization

Using the present spectroscopically confirmed sample of ultra-faint galaxies, we have the opportunity to put constraints on the UV luminosity function. We first describe the selection procedure of our sample and associated biases. The original sample has been selected in HFF studies^{24,47}, based on HST observation. The selection of the original photometric sample is based on Lyman break criteria, which identify the dropout because of continuum absorption by the neutral IGM blueward of Ly α . The photometric redshift through SED fitting was only measured to refine the redshift solution. Moreover, three sources were selected from the UNCOVER imaging data based on their photometric redshifts. Regarding these three sources, strong emission lines tend to help put stronger constraints on the photometric redshift estimates, resulting in narrower best-fit solutions, which could favour strong-line emitters in the sample selection⁷⁵. For the selection of this spectroscopic sample, we primarily focus on faint intrinsic magnitudes, typically $M_{\text{UV}} \gtrsim -17$ mag, as can be seen in Fig. 2. Their apparent magnitude ranges from $m_{\text{F150W}} = 27.4$ –29.7 AB mag. Although there is

an intentional bias to select intrinsically faint galaxies in this study, this is less the case regarding observed magnitudes. Finally, during the Multi-Shutter Assembly design, we assigned equal weights to all galaxies. Therefore, the only bias introduced here is the optimization of the number of sources that are included in one mask configuration. Therefore, galaxies that did not make it to the final sample were simply excluded for mask optimization reasons.

First, we compute an initial UV luminosity function based on the present sample binned in four magnitude bins and a survey volume, which depends on the original selection of the source. For the five HFF sources, we use the source plane effective volume²⁴ as a function of the magnitude bin. We rebin the original HFF sample to match the new magnitude bins. A scaling factor is then applied to the luminosity function points to match the HFF completeness-corrected counts. Finally, we apply a correction factor based on the success rate of the spectroscopic confirmation. For the three sources outside the HFF area, we recompute the source plane effective survey volume using the new lensing model and assuming a similar completeness function across the field. We perform the same exercise of rescaling the number counts in each magnitude bin. The final UV luminosity function is calculated by combining all galaxies with their associated corrected effective volume. Regarding uncertainties, we use the HFF volume uncertainties for the HFF sources and the updated volume uncertainties for the new sample, respectively. We note that the HFF uncertainties include systematic effects derived from a comparison between four independent models²⁴. For the three sources outside the HFF coverage, the comparison with another independent model¹³⁴ shows that the uncertainties are negligible for these small amplification factors. We also include Poisson errors and cosmic variance in the final luminosity function results. For the survey volume probed by our programme, we estimated cosmic variance to be around $\sigma_{\text{CV}} \sim 30\%$ (ref. 76). Overall, in Extended Data Fig. 3, we show that our measurements (orange points) are in good agreement with the faint end of the photometric UV luminosity function derived from HFF observations²⁴ (grey points).

In our efforts to determine whether galaxies can reionize the Universe, we proceed to calculate another crucial parameter: the production efficiency of ionizing radiation ξ_{ion} . This quantity is defined as the ratio between the LyC photon production rate in the units of s^{-1} , and the observed non-ionizing UV luminosity density L_{UV} estimated at 1,500 Å in units of $\text{erg s}^{-1} \text{Hz}^{-1}$:

$$\xi_{\text{ion}} = \frac{N(H^0)}{L_{\text{UV}}} (\text{erg}^{-1} \text{Hz}), \quad (1)$$

where $N(H^0)$ can be estimated from the H α Balmer line⁷⁷ assuming a case B recombination theory⁷⁸:

$$L(\text{H}\alpha) (\text{erg s}^{-1}) = 1.36 \times (1 - f_{\text{esc}}) 10^{-12} N(H^0) (\text{s}^{-1}) \quad (2)$$

where $L(\text{H}\alpha)$ is in units of erg s^{-1} and f_{esc} is the escape fraction of Lyman continuum radiation. In this calculation, we assume that $f_{\text{esc}} = 0$, meaning that all LyC photons are reprocessed into the Balmer lines. The derived ξ_{ion} value can be considered as a lower limit, because higher f_{esc} will lead to a higher ξ_{ion} . The H α emission line is not detected in source ID 18924. In this case, we use the H β luminosity and a case B conversion factor. Our measurements are reported in Fig. 3, together with literature results^{79–84}. These uncertainties due to potential field-to-field variations can also affect the ionizing properties of galaxies. We incorporated cosmic variance errors ($\sigma_{\text{UV}} \approx 30\%$) to the ξ_{ion} values for both $M_{\text{UV}} > -16.5$ mag and $M_{\text{UV}} < -16.5$ mag (Fig. 3).

Spectroscopic measurements in brighter galaxies have also reported ξ_{ion} values higher than canonical values⁸⁵. Several JWST studies have measured ξ_{ion} in faint galaxies at the epoch of reionization^{21,86}. However, their results are based on emission line fluxes inferred from broadband excess, rather than direct spectroscopic measurements. In particular,

JWST medium-band photometric data have been used to infer ξ_{ion} for galaxies over the redshift range $3 < z < 7$ (ref. 87). These measurements offer an opportunity to explore a larger population of galaxies through wide-area imaging. They report ionizing efficiencies in the range $\log[\xi_{\text{ion}} (\text{Hz erg}^{-1})] = 25.31\text{--}25.39$, in which galaxies with strong Ly α emission tend to have the highest values. These values are smaller than our average measurements for the faintest galaxies. However, most of their sample is at significantly lower redshifts. Their redshift distribution has two peaks at $z = 3$ and $z = 5$, and the median redshift of their sample is $z = 4.02$, which is well below the epoch of reionization. Among their sample of 370 galaxies, only about 25 galaxies lie within the epoch of reionization. Therefore, their average ξ_{ion} value is not representative of the epoch of reionization. Furthermore, this difference is smaller if we take into account the dynamic range of UV magnitudes explored in their study. Although they find a weak dependency of ξ_{ion} with M_{UV} , their sample consists of galaxies with UV magnitudes ranging from -23 mag to -15.5 mag, compared with our subsample of $M_{\text{UV}} > -16.5$ mag. Although imaging-based measurements can be complementary to spectroscopic studies, they have larger uncertainties (in the range $\sigma = 0.43\text{--}0.64$), because of the way emission line fluxes are inferred and are model-dependent, because the continuum is derived from SED fitting.

Finally, we derive constraints on the LyC escape fraction using indirect indicators calibrated in a large sample of nearby LyC-emitting galaxies. As the LyC emission is impossible to measure at the epoch of reionization, large efforts have been devoted in the past two decades to determine the escape fraction in $z < 4$ galaxies, and more importantly establish indirect methods, which can be transferable to reionization sources. This was precisely the motivation of the recent Low-redshift Lyman Continuum Survey (LzLCS)⁸⁸. Among the different physical properties of LyCleakers, the observed UV continuum slope β has been identified as a promising proxy of f_{esc} (ref. 26). Here we use the UV slopes derived from the best-fit models of Bagpipes and the LzLCS relation to infer f_{esc} . The derived values for the present sample range from 4.5% to 15.6%. Despite large uncertainties (around 50%), only two sources have f_{esc} values that can reach below 4% at 1σ .

Now with all three properties, we can assess the contribution of faint galaxies to cosmic reionization. We compute the ionizing photon emissivity of galaxies, which is the product of the total UV luminosity density ρ_{UV} derived from integrating the UV luminosity function and the production efficiency ξ_{ion} . The result will depend on the faint integration limit, which is set as the faintest bin of the spectroscopic luminosity function at $M_{\text{UV}} = -15$ mag. By multiplying this quantity by the escape fraction f_{esc} , we obtain the total ionizing photon rate density that is available to ionize the IGM. Down to $M_{\text{UV}} = -15$ mag, modest f_{esc} values around 5% are sufficient to maintain reionization.

We measure the gas-phase oxygen abundance using the strong optical lines diagnostic. Specifically, we use the $R3 = \log([\text{OIII}]\lambda 5007/\text{H}\beta)$ and adopt the most recent empirical calibrations at high-redshift^{89–91}. All of our sources show detections of $[\text{OIII}]\lambda 5007$ and $\text{H}\beta$. Furthermore, we also separate our sample into two bins according to the $\text{EW}(\text{H}\beta)$ at 100 \AA to account for ionization parameter variations⁸⁹. Also, for a given value of $R3$, the calibration defines two metallicity solutions. Although these sources probably have low metallicities, we use the $O32 = \log([\text{OIII}]\lambda 4949,5007/[\text{OII}]\lambda 3727,3729)$ ratio to distinguish between the two branches. For most of the sources, the $[\text{OII}]$ is not detected, which provides a lower limit on $O32$, which is found to vary in the range $O32 = [0.7\text{--}1.4]$. Using the $O32$ metallicity indicator, the resulting values are all compatible with the low-metallicity branch solution. The metallicity measurements are reported in Table 2.

Apart from the physical properties that may ease the escape of ionizing photons from these galaxies, metallicity can also inform us of the ionizing properties of this population. We measured the gas-phase metallicity using the $R3 = [\text{OIII}]/\text{H}\beta$ line ratio based on the most recent calibrations⁹². We find extremely low metallicities, ranging from $12 + \log(\text{O/H}) = 6.70\text{--}7.46$, which corresponds to 1–6%

of the solar metallicity. These low metallicities are often suggestive of strong ionizing radiation from massive stars⁹³. At the same time, these distant low-mass galaxies, considered as the building blocks of present-day galaxies, are expected to be metal-poor, owing to their supposedly pristine gas conditions. We note that our estimate relies on the calibration of strong line diagnostics, which are prone to significant uncertainties at $z > 6$. On average, these estimates lie at 1σ to 2σ intervals from each other.

Size measurements

To further characterize these sources, we measure their sizes by fitting their morphology in the NIRCam F150W filter with a Sérsic profile⁹⁴. Measurements of the half-light radii for all eight galaxies are performed using the pysersic⁹⁵ package. For each source, we assume a single Sérsic profile and mask all nearby sources in the photometric catalogue³⁸. The priors for the half-light radius, Sérsic index, axis ratio and position angle are all uniform and varied from 0.5 to 10 pixels, 0.65 to 4, 0.1 to 1 and 0 to -2π respectively. Central position and flux of the priors are represented as Gaussian distributions with the location and width based on the photometric catalogue³⁸. A flat sky background is fit simultaneously. The posterior distribution is explored using the No-U-Turn (NUTS)⁹⁶ sampler implemented in numpyro⁹⁷ with two chains for 1,000 warm-up and sampling steps each.

Several of our objects are significantly distorted by gravitational lensing, which means that we need to take the shear into account when deriving the half-light radius. To do that, we use our lensing model to derive the tangential and radial magnifications, defined as $\mu = \mu_t\mu_r$, from the deflection field at the position and redshift of each source. As our objects are sheared along the tangential direction, we use the tangential component of the magnification to correct the half-light radii.

The derived effective radii, corrected for magnification and taking the shear into account, vary between $r_{\text{eff}} = 30\text{--}300$ pc. Overall, these constraints show that these sources are small, in broad agreement with an extrapolation to lower masses of the size–mass relation derived at similar redshifts⁹⁸, albeit with significant scatter. These small sizes and high SSFRs also support the scenario of stochastic star-formation histories in these systems or dust ejection⁹⁹, because of their small dynamical time and low gravitational potential.

Data availability

The NIRCam and HST imaging data are available on the UNCOVER webpage at GitHub (<https://jwst-uncover.github.io/>). The NIRSpec spectroscopic data are publicly available through the Mikulski Archive for Space Telescopes (MAST; <https://archive.stsci.edu/>), under programme ID 2561. The UNCOVER lensing products are available at GitHub (<https://jwst-uncover.github.io/DR1.html#LensingMaps>).

Code availability

The following codes were used in this study: Astropy^{100,101}, Bagpipes^{58,59}, BEAGLE⁶⁹, EAzY⁴⁹, Matplotlib¹⁰², msaexp v.0.6.10¹⁰³, NumPy¹⁰⁴, NUTS^{97,105}, PyMultinest^{67,68}, pysersic⁹⁵, SciPy¹⁰⁶ and GrizLi (<https://github.com/gbrammer/grizli>).

36. Oke, J. B. & Gunn, J. E. Secondary standard stars for absolute spectrophotometry. *Astrophys. J.* **266**, 713–717 (1983).
37. Bezanson, R. et al. The JWST UNCOVER Treasury survey: Ultradeep NIRSpec and NIRCam ObserVations before the Epoch of Reionization. Preprint at <https://doi.org/10.48550/arXiv.2212.04026> (2022).
38. Weaver, J. R. et al. The UNCOVER Survey: a first-look HST + JWST Catalog of 60,000 galaxies near A2744 and beyond. *Astrophys. J. Suppl. Ser.* **270**, 7 (2024).
39. Rieke, M. J. et al. Performance of NIRCam on JWST in Flight. *Publ. Astron. Soc. Pacific* **135**, 028001 (2023).
40. Brammer, G. Grizli: Grism redshift and line analysis software. Astrophysics Source Code Library, record ascl:1905.001 (2019).
41. Lotz, J. M. et al. The Frontier Fields: survey design and initial results. *Astrophys. J.* **837**, 97 (2017).

Article

42. Steinhardt, C. L. et al. The BUFFALO HST Survey. *Astrophys. J. Suppl. Ser.* **247**, 64 (2020).
43. Jakobsen, P. et al. The Near-Infrared Spectrograph (NIRSpec) on the James Webb Space Telescope. I. Overview of the instrument and its capabilities. *Astron. Astrophys.* **661**, A80 (2022).
44. Ferruit, P. et al. The Near-Infrared Spectrograph (NIRSpec) on the James Webb Space Telescope. II. Multi-object spectroscopy (MOS). *Astron. Astrophys.* **661**, A81 (2022).
45. Heintz, K. E. et al. Extreme damped Lyman- α absorption in young star-forming galaxies at $z=9\text{--}11$. Preprint at <https://doi.org/10.48550/arXiv.2306.00647> (2023).
46. Horne, K. An optimal extraction algorithm for CCD spectroscopy. *Publ. Astron. Soc. Pacific* **98**, 609–617 (1986).
47. Bouwens, R. J., Illingworth, G., Ellis, R. S., Oesch, P. & Stefanon, M. $z\sim 2\text{--}9$ galaxies magnified by the Hubble Frontier Field clusters. II. Luminosity functions and constraints on a faint-end turnover. *Astrophys. J.* **940**, 55 (2022).
48. Brammer, G., Strait, V., Matharu, J. & Momcheva, I. grizli. Zenodo zenodo.org/records/6672538 (2022).
49. Brammer, G. B., van Dokkum, P. G. & Coppi, P. EAZY: a fast, public photometric redshift code. *Astrophys. J.* **686**, 1503–1513 (2008).
50. Zitrin, A. et al. Hubble Space Telescope combined strong and weak lensing analysis of the CLASH sample: mass and magnification models and systematic uncertainties. *Astrophys. J.* **801**, 44 (2015).
51. Pascale, M. et al. Unscrambling the lensed galaxies in JWST images behind SMACS 0723. *Astrophys. J. Lett.* **938**, L6 (2022).
52. Bacon, R. et al. The MUSE second-generation VLT instrument. In *Ground-based and Airborne Instrumentation for Astronomy III*, Vol. 7735 of *Society of Photo-Optical Instrumentation Engineers (SPIE) Conference Series* (eds McLean, I. S. et al.) 773508 (SPIE, 2010).
53. Mahler, G. et al. Strong-lensing analysis of A2744 with MUSE and Hubble Frontier Fields images. *Mon. Not. R. Astron. Soc.* **473**, 663–692 (2018).
54. Richard, J. et al. An atlas of MUSE observations towards twelve massive lensing clusters. *Astron. Astrophys.* **646**, A83 (2021).
55. Bergamini, P. et al. The GLASS-JWST Early Release Science Program. III. Strong-lensing model of Abell 2744 and its infalling regions. *Astrophys. J.* **952**, 84 (2023).
56. Zitrin, A. et al. Ly α emission from a luminous $z=8.68$ galaxy: implications for galaxies as tracers of cosmic reionization. *Astrophys. J. Lett.* **810**, L12 (2015).
57. Furtak, L. J. et al. Constraining the physical properties of the first lensed $z\sim 9\text{--}16$ galaxy candidates with JWST. *Mon. Not. R. Astron. Soc.* **519**, 3064–3075 (2023).
58. Carnall, A. C., McLure, R. J., Dunlop, J. S. & Davé, R. Inferring the star formation histories of massive quiescent galaxies with BAGPIPES: evidence for multiple quenching mechanisms. *Mon. Not. R. Astron. Soc.* **480**, 4379–4401 (2018).
59. Carnall, A. C. et al. The VANDELS survey: the star-formation histories of massive quiescent galaxies at $1.0 < z < 1.3$. *Mon. Not. R. Astron. Soc.* **490**, 417–439 (2019).
60. Curtis-Lake, E. et al. Spectroscopic confirmation of four metal-poor galaxies at $z=10.3\text{--}13.2$. *Nat. Astron.* **7**, 622–632 (2023).
61. Bruzual, G. & Charlot, S. Stellar population synthesis at the resolution of 2003. *Mon. Not. R. Astron. Soc.* **344**, 1000–1028 (2003).
62. Sánchez-Blázquez, P. et al. Medium-resolution Isaac Newton Telescope library of empirical spectra. *Mon. Not. R. Astron. Soc.* **371**, 703–718 (2006).
63. Falcón-Barroso, J. et al. An updated MILES stellar library and stellar population models. *Astron. Astrophys.* **532**, A95 (2011).
64. Ferland, G. J. et al. The 2017 Release Cloudy. *Rev. Mex. Astron. Astrofis.* **53**, 385–438 (2017).
65. Charlot, S. & Fall, S. M. A simple model for the absorption of starlight by dust in galaxies. *Astrophys. J.* **539**, 718–731 (2000).
66. Papovich, C. et al. CEERS key paper. V. Galaxies at $4 < z < 9$ are bluer than they appear—characterizing galaxy stellar populations from rest-frame $\sim 1\mu\text{m}$ imaging. *Astrophys. J. Lett.* **949**, L18 (2023).
67. Buchner, J. et al. X-ray spectral modelling of the AGN obscuring region in the CDFS: Bayesian model selection and catalogue. *Astron. Astrophys.* **564**, A125 (2014).
68. Feroz, F., Hobson, M. P., Cameron, E. & Pettitt, A. N. Importance nested sampling and the MultiNest algorithm. *Open J. Astrophys.* **2**, 10 (2019).
69. Chevallard, J. & Charlot, S. Modelling and interpreting spectral energy distributions of galaxies with BEAGLE. *Mon. Not. R. Astron. Soc.* **462**, 1415–1443 (2016).
70. Ferland, G. J. et al. The 2013 Release of Cloudy. *Rev. Mex. Astron. Astrofis.* **49**, 137–163 (2013).
71. Gutkin, J., Charlot, S. & Bruzual, G. Modelling the nebular emission from primeval to present-day star-forming galaxies. *Mon. Not. R. Astron. Soc.* **462**, 1757–1774 (2016).
72. Chabrier, G. Galactic stellar and substellar initial mass function. *Publ. Astron. Soc. Pacific* **115**, 763–795 (2003).
73. Pei, Y. C. Interstellar dust from the Milky Way to the magellanic clouds. *Astrophys. J.* **395**, 130–139 (1992).
74. Inoue, A. K., Shimizu, I., Iwata, I. & Tanaka, M. An updated analytic model for attenuation by the intergalactic medium. *Mon. Not. R. Astron. Soc.* **442**, 1805–1820 (2014).
75. Roberts-Borsani, G. et al. $z\geq 7$ galaxies with Red Spitzer/IRAC [3.6]–[4.5] colors in the full CANDELS data set: the brightest-known galaxies at $z\sim 7\text{--}9$ and a probable spectroscopic confirmation at $z=7.48$. *Astrophys. J.* **823**, 143 (2016).
76. Trenti, M. & Stiavelli, M. Cosmic variance and its effect on the luminosity function determination in deep high- z surveys. *Astrophys. J.* **676**, 767–780 (2008).
77. Leitherer, C. & Heckman, T. M. Synthetic properties of starburst galaxies. *Astrophys. J. Suppl. Ser.* **96**, 9 (1995).
78. Osterbrock, D. E. *Astrophysics of Gaseous Nebulae and Active Galactic Nuclei* (Univ. Science Books, 1989).
79. Atek, H. et al. The star formation burstiness and ionizing efficiency of low-mass galaxies. *Mon. Not. R. Astron. Soc.* **511**, 4464–4479 (2022).
80. Bouwens, R. J. et al. The Lyman-continuum photon production efficiency ξ_{ion} of $z=4\text{--}5$ galaxies from IRAC-based H α measurements: implications for the escape fraction and cosmic reionization. *Astrophys. J.* **831**, 176 (2016).
81. Matthee, J. et al. The production and escape of Lyman-continuum radiation from star-forming galaxies at $z=2$ and their redshift evolution. *Mon. Not. R. Astron. Soc.* **465**, 3637–3655 (2017).
82. Nanayakkara, T. et al. Reconstructing the observed ionizing photon production efficiency at $z=2$ using stellar population models. *Astrophys. J.* **889**, 180 (2020).
83. Matthee, J. et al. EIGER. II. First spectroscopic characterization of the young stars and ionized gas associated with strong H β and [O III] line emission in galaxies at $z=5\text{--}7$ with JWST. *Astrophys. J.* **950**, 67 (2023).
84. Sun, F. et al. First sample of H α +[O III] $\lambda\lambda 5007$ line emitters at $z>6$ through JWST/NIRCam slitless spectroscopy: physical properties and line-luminosity functions. *Astrophys. J.* **953**, 53 (2023).
85. Tang, M. et al. JWST/NIRSpec spectroscopy of $z=7\text{--}9$ star-forming galaxies with CEERS: new insight into bright Ly α emitters in ionized bubbles. *Mon. Not. R. Astron. Soc.* **526**, 1657–1686 (2023).
86. Saxena, A. et al. JADES: The production and escape of ionizing photons from faint Lyman-alpha emitters in the epoch of reionization. Preprint at <https://doi.org/10.48550/arXiv.2306.04536> (2023).
87. Prieto-Lyon, G. et al. The production of ionizing photons in UV-faint $z=3\text{--}7$ galaxies. *Astron. Astrophys.* **672**, A186 (2023).
88. Flury, S. R. et al. The low-redshift Lyman Continuum Survey. I. New, diverse local Lyman continuum emitters. *Astrophys. J. Suppl. Ser.* **260**, 1 (2022).
89. Nakajima, K. et al. EMPRESS. V. Metallicity diagnostics of galaxies over $12 + \log(\text{O/H}) \simeq 6.9\text{--}8.9$ established by a local galaxy census: preparing for JWST spectroscopy. *Astrophys. J. Suppl. Ser.* **262**, 3 (2022).
90. Nakajima, K. et al. EMPRESS. VI. Metallicity diagnostics of galaxies over $12 + \log(\text{O/H}) = 6.9\text{--}8.9$ established by a local galaxy census: preparing for JWST spectroscopy. *Astrophys. J. Suppl. Ser.* **262**, 3 (2022).
91. Sanders, R. L. et al. The MOSDEF survey: the evolution of the mass-metallicity relation from $z=0$ to $z\sim 3.3$. *Astrophys. J.* **914**, 19 (2021).
92. Sanders, R. L., Shapley, A. E., Topping, M. W., Reddy, N. A. & Brammer, G. B. Direct T_e -based metallicities of $z=2\text{--}9$ galaxies with JWST/NIRSpec: empirical metallicity calibrations applicable from reionization to cosmic noon. Preprint at <https://doi.org/10.48550/arXiv.2303.08149> (2023).
93. Stanway, E. R. & Eldridge, J. J. Initial mass function variations cannot explain the ionizing spectrum of low metallicity starbursts. *Astron. Astrophys.* **621**, A105 (2019).
94. Sérsic, J. L. Influence of the atmospheric and instrumental dispersion on the brightness distribution in a galaxy. *Bol. Asoci. Argentina Astron. Plata Argentina* **6**, 41–43 (1963).
95. Pasha, I. & Miller, T. B. pysisic: a Python package for determining galaxy structural properties via Bayesian inference, accelerated with jax. *J. Open Source Software* **8**, 5703 (2023).
96. Hoffman, M. D. & Gelman, A. et al. The No-U-Turn sampler: adaptively setting path lengths in Hamiltonian Monte Carlo. *J. Mach. Learn. Res.* **15**, 1593–1623 (2014).
97. Phan, D., Pradhan, N. & Jankowiak, M. Composable effects for flexible and accelerated probabilistic programming in NumPyro. Preprint at <https://arxiv.org/abs/1912.11554> (2019).
98. Holwerda, B. W. et al. The sizes of candidate $z=9\text{--}10$ galaxies: confirmation of the bright CANDELS sample and relation with luminosity and mass. *Astrophys. J.* **808**, 6 (2015).
99. Ferrara, A., Pallottini, A. & Dayal, P. On the stunning abundance of super-early, luminous galaxies revealed by JWST. *Mon. Not. R. Astron. Soc.* **522**, 3986–3991 (2023).
100. Astropy Collaboration. et al. Astropy: a community Python package for astronomy. *Astron. Astrophys.* **558**, A33 (2013).
101. Astropy Collaboration. et al. The Astropy Project: building an open-science project and status of the v2.0 core package. *Astron. J.* **156**, 123 (2018).
102. Hunter, J. D. Matplotlib: a 2D graphics environment. *Comput. Sci. Eng.* **9**, 90–95 (2007).
103. Brammer, G. msaexp: NIRSpec analysis tools. Zenodo <https://zenodo.org/records/8314675> (2022).
104. Harris, C. R. et al. Array programming with NumPy. *Nature* **585**, 357–362 (2020).
105. Hoffman, M. D. & Gelman, A. The No-U-Turn sampler: adaptively setting path lengths in Hamiltonian Monte Carlo. Preprint at <https://doi.org/10.48550/arXiv.1111.4246> (2011).
106. Virtanen, P. et al. SciPy 1.0: fundamental algorithms for scientific computing in Python. *Nat. Methods* **17**, 261–272 (2020).

Acknowledgements H.A. and I.C. acknowledge support from CNES, focused on the JWST mission and the Programme National Cosmology and Galaxies (PNCG) of CNRS/INSU with INP and IN2P3, co-funded by CEA and CNES. H.A. thanks the Cosmic Dawn Center (DAWN) for their support. DAWN is funded by the Danish National Research Foundation (grant no. 140). I.L. acknowledges support from the Australian Research Council through Future Fellowship FT2020010798. P.D. acknowledges support from the NWO (grant no. 016.VIDI.189.162) (ODIN) and from the CO-FUND Rosalind Franklin programme of the European Commission and the University of Groningen. A.Z. acknowledges support from the US-Israel Binational Science Foundation (BSF) (grant no. 2020750), the US National Science Foundation (NSF) (grant no. 2109066) and the Ministry of Science and Technology, Israel. The work of C.C.W. is supported by NOIRLab, which is managed by the Association of Universities for Research in Astronomy (AURA) under a cooperative agreement with the NSF.

Author contributions H.A. led the analysis and writing of the paper. L.J.F. and A.Z. constructed the lens model and extracted lensing-related quantities. S.F. produced the figures. I.L. and R.B. are the principal investigators of the UNCOVER programme. R.B. and I.L. designed the observations and reduced the spectra. J.R.W. and B.W. produced the catalogues used for target selection. P.D. provided simulations to interpret the observational results obtained. V.K. produced line measurements. I.C. estimated survey volumes. D.J.S. ran an SED fitting analysis. T.B.M. measured the galaxy sizes. All authors contributed to the paper and aided the analysis and interpretation.

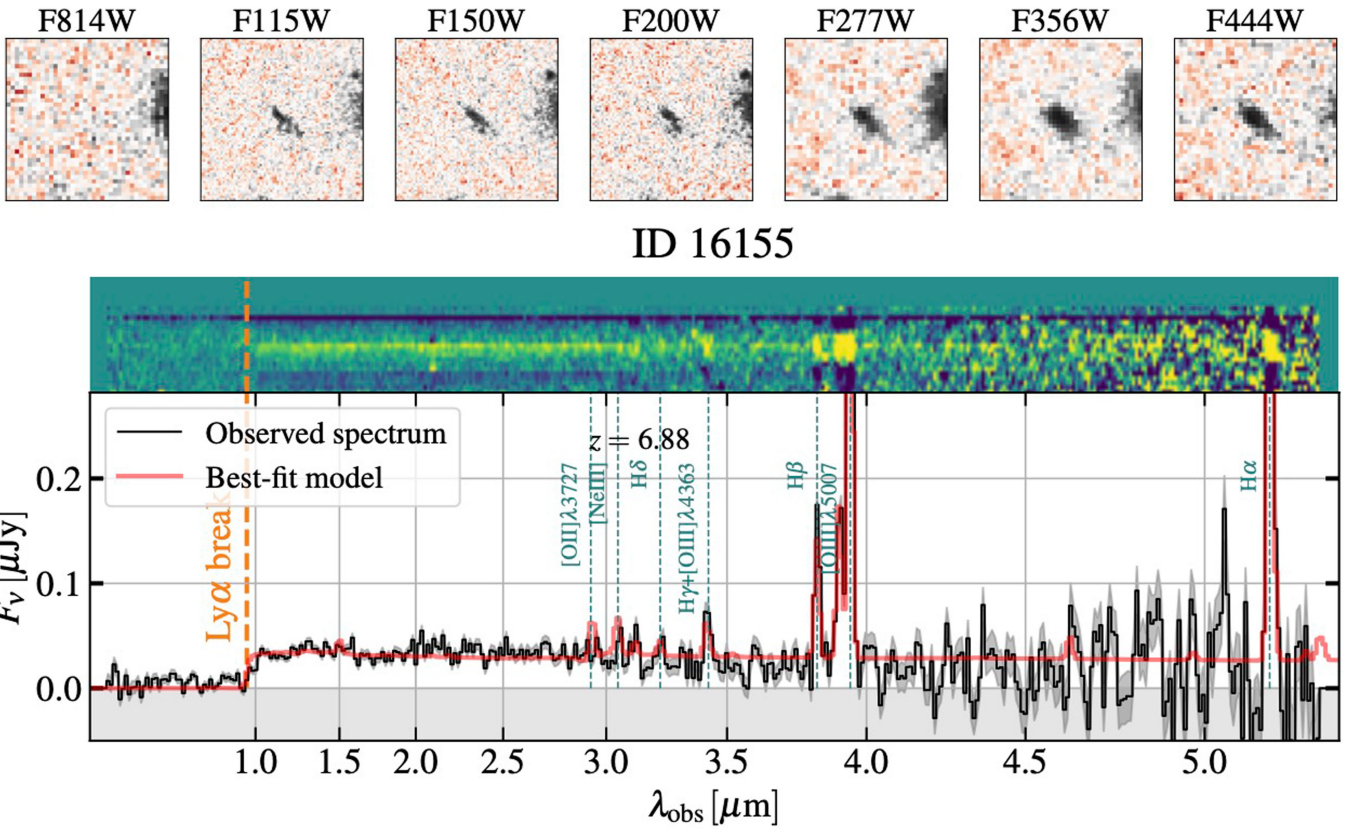
Competing interests The authors declare no competing interests.

Additional information

Correspondence and requests for materials should be addressed to Hakim Atek.

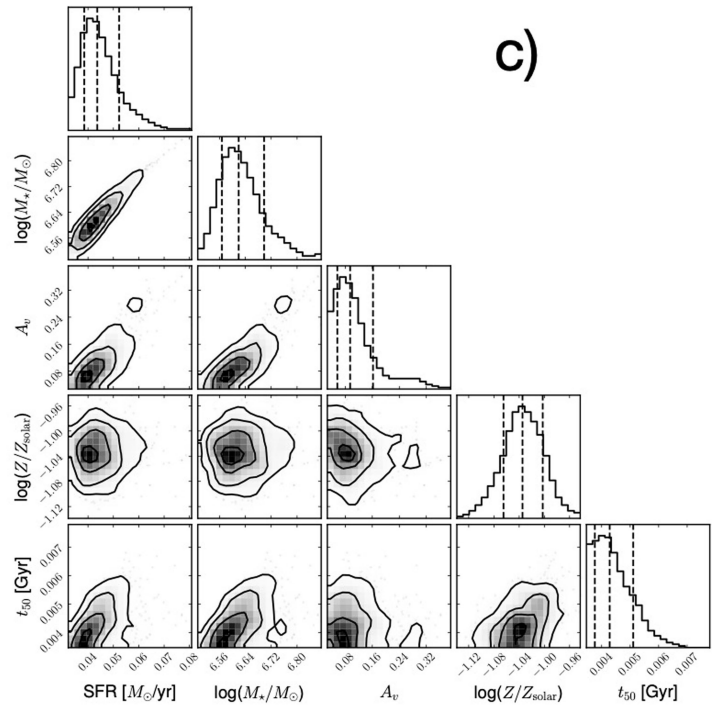
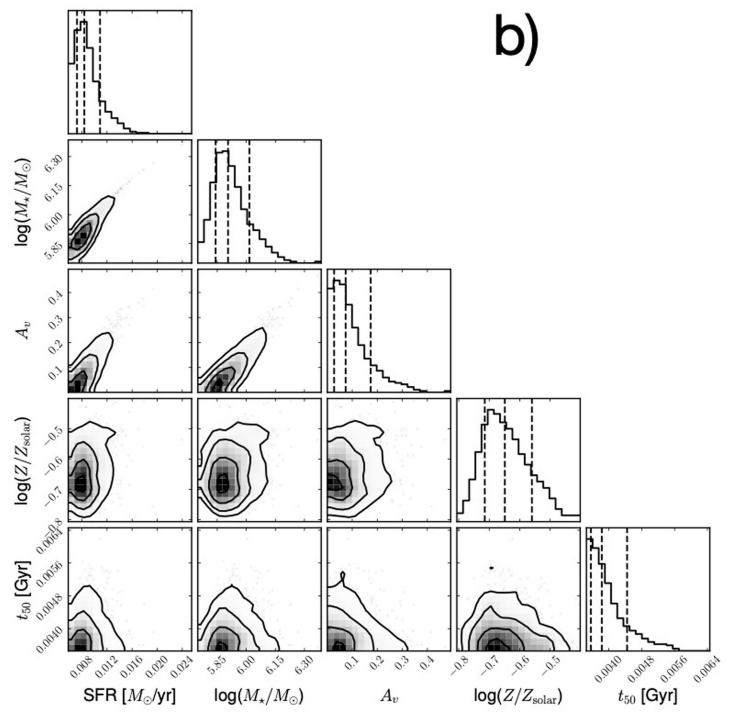
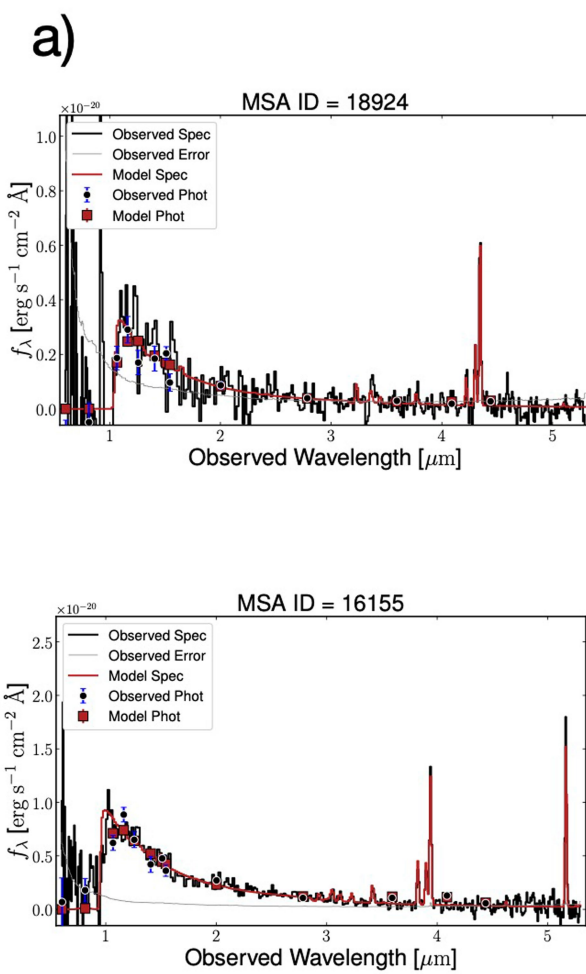
Peer review information *Nature* thanks the anonymous reviewers for their contribution to the peer review of this work.

Reprints and permissions information is available at <http://www.nature.com/reprints>.



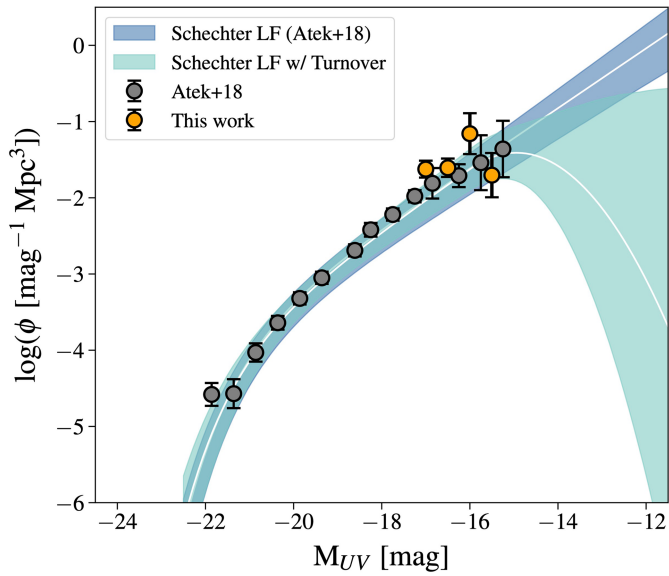
Extended Data Fig. 1 | UNCOVERJWST data for galaxy 16155 at $z_{\text{spec}} = 6.88$. The top panels show image cutouts in seven different filters at increasing wavelength including ancillary HST/ACS data in F814W, and UNCOVERJWST imaging in F115W, F150W, F200W, F277W, F356W, and F444W bands (left to right). The central panel shows the UNCOVER NIRSpec data, with the 2D spectrum on top of the 1D optimally extracted spectrum (black with gray $1-\sigma$

uncertainty ranges). The red lines show the best-fit msaexp template spectrum. The observed-frame wavelengths of key emission lines are indicated as vertical dashed lines. The bottom panels show a zoomed in version of three different parts of the spectrum around the Ly α break (left), around the [OIII]+H β emission lines (middle) and the H α line (right).



Extended Data Fig. 2 | Stellar population simultaneous fitting to the NIRSpec spectra and NIRCam photometry. **Panel a:** Two representative sources (IDs 18924 and 16155) are shown. The best-fit Bagpipes model (red curve) is plotted over the observed NIRSpec spectrum (black curve), together with the error spectrum (gray curve). The NIRCam photometric measurements

are represented with black points with their associated 1-sigma uncertainties. **Panel b:** Posterior distribution function for the main physical properties of ID 16155. When relevant, the parameters are corrected for magnification. **Panel c:** Same as panel b, for source ID 18924.



Extended Data Fig. 3 | Spectroscopic constraints on the UV luminosity function.

The UV luminosity function as determined from our spectroscopic sample is represented by orange points. Also shown, the photometric determination from the HFF data²⁴, together with the best-fit Schechter function (blue curve) and a modified Schechter with a potential turnover (teal curve). The shaded region of each curve represent the $1 - \sigma$ uncertainties.